Check for updates



ADVANCED FUNCTIONAL MATERIALS
www.afm-journal.de

# High Power Density $Ag_2Se/Sb_{1.5}Bi_{0.5}Te_3$-Based Fully Printed Origami Thermoelectric Module for Low-Grade Thermal Energy Harvesting

*Leonard Franke,* Andres Georg Rösch, Muhammad Irfan Khan, Qihao Zhang, Zhongmin Long, Irene Brunetti, Matías Nicolas Joglar, Ana Moya Lara, Claudia Delgado Simão, Holger Geßwein, Alexei Nefedov, Yolita M. Eggeler, Uli Lemmer,* and Md Mofasser Mallick**

**Printing technologies have the potential to reduce the manufacturing costs of many electronic devices significantly. Here, a scalable manufacturing route for high-performance fully printed thermoelectric generators (TEGs) as a cost-effective solution for energy harvesting is demonstrated. This work presents a facile one-pot synthesis method to develop a high-performance $Ag_2Se$-based n-type paste, which is used to fabricate a fully printed origami TEG by employing the $Ag_2Se$-based material for the n-type legs and a previously reported Bi-Sb-Te-based paste for the p-type legs. The n-type film exhibits a power factor of 13.5 μW cm$^{-1}$ K$^{-2}$ and a maximum figure-of-merit (ZT) of ≈ 0.92. Furthermore, printable carbon paste is introduced as an effective interface between the thermoelectric and electrode materials, which reduces the contact resistances in the thermoelectric device. The origami folded TEG exhibits an open-circuit voltage ($V_{OC}$) of 284 mV, a power output of 370.88 μW, and an exceptionally high power density ($p_{max}$) of 10.72 Wm$^{-2}$ at a temperature difference (ΔT) of 80.7 K, considering that the TEG fabrication does not involve any pressure treatment and vacuum sintering. These results underscore the scalability of the presented manufacturing process and the capability of printed origami TEGs for powering the Internet of Things (IoT) with low-grade waste heat.**

## 1. Introduction

Most usable waste heat is dissipated as low-grade heat at temperatures below 100 °C.[1] TEGs represent a promising technology that can make use of this waste heat. The printing of thermoelectric (TE) devices can thereby facilitate very cost-effective and shape-conformable manufacturing,[2] allowing the potential production of inexpensive large-area TEGs or a large throughput of TE devices. One challenge for TEGs produced by printing technologies is the manufacture of devices that can deliver sufficient power in the range of 50–100 μW[3] for the Internet of Things (IoT) from a low-grade heat source. Therefore, developing high-performance printed TE materials and fabricating high-power density TE modules comprising the same are crucial steps toward the implementation of printed TEGs for IoT applications. However, printing TE materials and achieving high performance

L. Franke, A. Georg Rösch, M. I. Khan, Q. Zhang, I. Brunetti, U. Lemmer, M. M. Mallick
Light Technology Institute
Karlsruhe Institute of Technology (KIT)
76131 Karlsruhe, Germany
E-mail: leonard.franke@kit.edu; uli.lemmer@kit.edu; mofasser.mallick@kit.edu

Z. Long, Y. M. Eggeler
Laboratory for Electron Microscopy
Karlsruhe Institute of Technology (KIT)
76131 Karlsruhe, Germany

The ORCID identification number(s) for the author(s) of this article can be found under https://doi.org/10.1002/adfm.202403646

© 2024 The Author(s). Advanced Functional Materials published by Wiley-VCH GmbH. This is an open access article under the terms of the Creative Commons Attribution-NonCommercial License, which permits use, distribution and reproduction in any medium, provided the original work is properly cited and is not used for commercial purposes.

**DOI: 10.1002/adfm.202403646**

I. Brunetti, U. Lemmer
InnovationLab GmbH
Speyerer Strasse 4, 69115 Heidelberg, Germany

M. N. Joglar, A. M. Lara, C. D. Simão
Eurecat Centre Tecnològic de Catalunya Functional Printing and Embedded Devices Unit Mataró
Catalonia 08302, Spain

H. Geßwein
Institut für Angewandte Materialien (IAM-ESS)
Karlsruhe Institute of Technology (KIT)
Hermann-von-Helmholtz-Platz 1D, 76344 Eggenstein-Leopoldshafen, Germany

A. Nefedov
Institute of Functional Interfaces
Karlsruhe Institute of Technology (KIT)
76344 Eggenstein-Leopoldshafen, Germany

U. Lemmer
Institute of Microstructure Technology
Karlsruhe Institute of Technology (KIT)
76344 Eggenstein-Leopoldshafen, Germany

poses a major challenge in the field of printed thermoelectrics.[4–6] As for the printing process, the material needs to exhibit good processability in the form of a paste or ink, while in the final device, the solid-state TE material properties are pivotal. It is challenging to fulfill these requirements simultaneously, especially for the electrical conductivity ($\sigma$), since many inorganic materials require high-temperature sintering to ensure low electric resistance of the TE film. The presence of binders, solvents, and additives in TE particle-based printed materials usually raises interfacial resistances due to the grain boundaries in the film, leading to a lower ZT. Therefore, conventional bulk thermoelectric devices still outperform printed devices. However, recent material research conducted on inorganic and inorganic/organic hybrid printable TE materials on Ag2Se and Bi-Te,[7–12] has led to higher efficiencies and has reduced the performance gap between bulk and printed TE devices.[13,14] It should be noted that despite the development of high-performance printed TE materials, improper fabrication or an unfavorable material selection can result in high resistances, causing Joule heating which diminishes the power output of the device. Therefore, it is paramount to develop a pair of optimized n- and p-type materials and then fabricate the printed TEGs in a manner that minimizes contact resistances in the device. Similar to bulk TEGs, the selection of the right contacting material has a large influence on the final device performance, e.g., a direct contacting of printed Bi-Sb-Te with silver or copper pastes usually results in significant contact resistances diminishing the output power of the device.[15,16] Therefore, selecting a suitable interface material is crucial for manufacturing a printed TEG. A common method for printed TEGs, similar to bulk TE devices, is to apply a Ni interface between the electrode and the TE film.[17] However, this usually requires a time-consuming sputtering process, making scalable production more difficult.

In this study, we report an alternative manufacturing route for a fully printed n-type Ag-Se/p-type Bi-Sb-Te-based TEG, investigating a selection of printable interface materials to reduce contact resistance in the device. For the n-type Ag-Se TE material, we introduce a new synthesis route adopting the same one-pot method developed for the p-type material.[10] The characterization of the n-type film revealed a high figure of merit (ZT = 0.92) comparable to what was previously reported.[3] A conductive carbon paste between the TE materials and conducting electrodes yielded the lowest interface resistances in this study and proved to be an effective method for achieving high-performance devices. We utilized the same screen-printing method for all materials, demonstrating the scalability of the process. For the sintering of the TE material, we apply two different pressure-free sintering techniques. While the n-type silver selenide (Ag—Se) is sintered at a low temperature (473 K) in the ambient atmosphere on a hot plate,[18] the dried p-type bismuth telluride (Bi—Sb—Te) film is sintered at higher temperatures via pulsed photonic curing.[19] Utilizing and optimizing this new manufacturing route (**Figure 1a–e**), we produced and characterized an origami-inspired folded TE module (Figure 1–5) as Figure 6,7 it was introduced by Rösch et al.[13] and evaluated the device performance for low-grade energy harvesting for powering IoT devices.

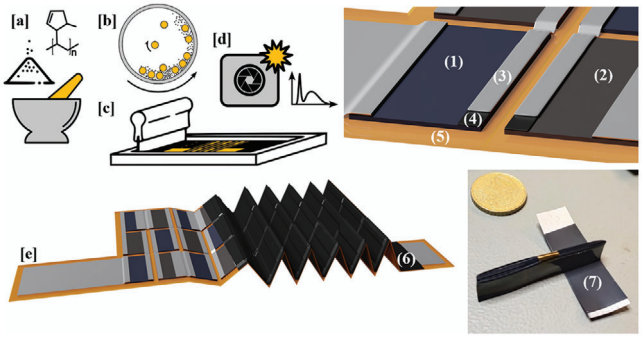


**Figure 1.** Schematics of the fully printed origami thermoelectric module (origami TEG). Manufacturing steps: a) one-pot synthesis, b) planetary ball milling, c) screen-printing, d) pulsed photonic curing, e) folding; Device structure: 1) n-type (Ag-Se), 2) p-type (Bi-Sb-Te), 3) electrodes (Ag), 4) interface material (conductive carbon), 5) substrate (PI), 6) encapsulation & electrode insulation, 7) folded Origami-TEG with a 50 $€_{ct}$ coin as reference.

## 2. Result

### 2.1. Crystallography and Microstructural Characterization of Printed n-type Film

**Figure 2a** shows the X-ray diffraction (XRD) patterns of $Ag_2Se$ films that were prepared according to the new synthesis route for screen printable $Ag_2Se$ described in 5.2. After drying, the printed film shows mixed phases of elemental Ag, Se, and the main phase orthorhombic $\beta$-$Ag_2Se$. These results follow previous reports that the orthorhombic $\beta$-$Ag_2Se$ phase can be formed during magnetic stirring by a dissociative adsorption reaction of Se and Ag even at ambient temperature.[20] As there are still some unreacted Ag and Se phases, we sintered the film at 473 K to complete the reaction and densify the films. The temperature was set based on our previous temperature-dependent XRD results.[8] After sintering, the peaks of the Ag and Se phases become insignificant. Furthermore, Rietveld refinement analysis of the XRD pattern of the sintered film was performed. The fitting parameters R-Factor and $\chi^2$ are found to be 4.18 and 1.99 respectively. Figure 2b shows that the sintered film corresponds to orthorhombic $\beta$-$Ag_2Se$ with the $P2_12_12_1$ space group with a small fraction of excess Ag. There are two structurally different sites of Ag ions: Ag(1) is coordinated by four selenium atoms in a distorted tetrahedral arrangement, whereas Ag(2) is coordinated by three selenium atoms in a trigonal planar arrangement. The lattice parameters of the $\beta$-$Ag_2Se$ phase are estimated to be $a$ = 0.4334(4) nm, $b$ = 0.7067(6), and $c$ = 0.7774(7) nm. The Ag3d detailed XP spectrum (Figure 2c) consists of one doublet with a fixed splitting of 6 eV, keeping the intensity ratio of 3:2 between Ag $3d_{5/2}$ and Ag $3d_{3/2}$ lines. The position of the Ag $3d_{3/2}$ lines at 367.9 eV is in good agreement with the $Ag^+$ oxidation state, which is typical for $Ag_2Se$,[21,22] No additional component (corresponding to $Ag^0$ state) at 368.3 eV as, well any broadening of the Ag $3d_{5/2}$ line could be recognized in the measured spectrum. The combined Se3d+Ag4p XP spectra are presented in **Figure 3b**. This detailed spectrum was deconvoluted with unresolved Ag4p peak and Se3d doublet (the splitting of 0.86 eV, intensity ratio of 3:2 in accordance with


© 2024 The Author(s). Advanced Functional Materials published by Wiley-VCH GmbH

16163028, 0, Downloaded from https://onlinelibrary.wiley.com/doi/10.1002/adfm.202403646 by Karlsruher Institut F., Wiley Online Library on [27/06/2024]. See the Terms and Conditions (https://onlinelibrary.wiley.com/terms-and-conditions) on Wiley Online Library for rules of use; OA articles are governed by the applicable Creative Commons License

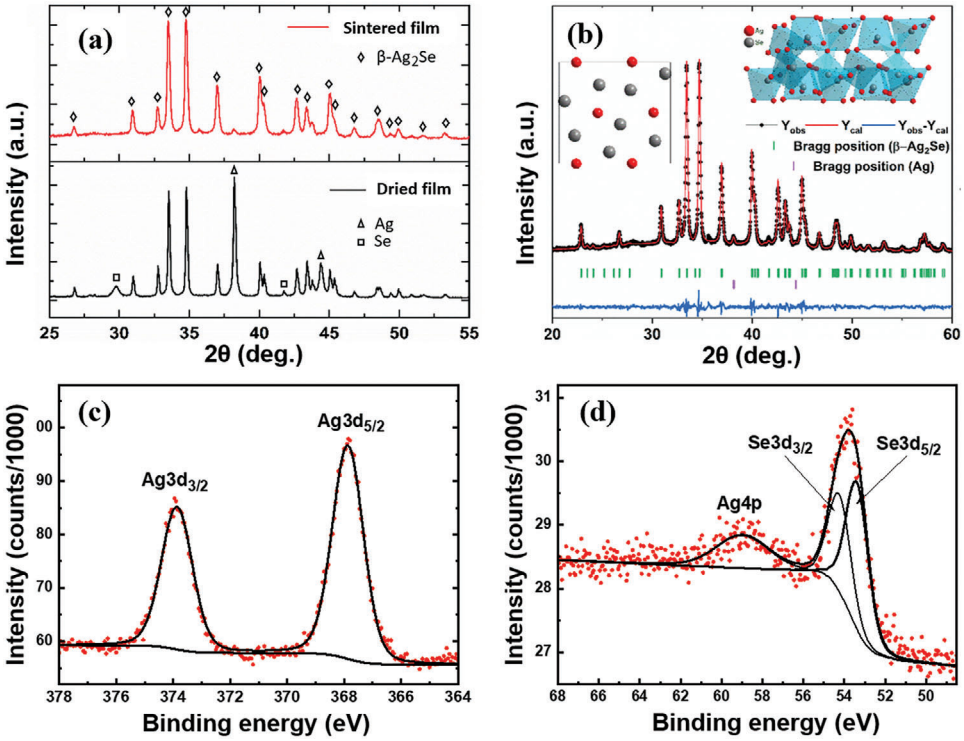


**Figure 2.** a) XRD patterns of the printed films. b) Rietveld refinement results of the printed film after sintering at 473 K. XPS results of the $Ag_2Se$ film: c) Ag3d core-level spectra; d) Se3d and Ag4p core-level spectra. The red dots show the experimental spectra and the black curves represent the deconvolution of independent components and background.

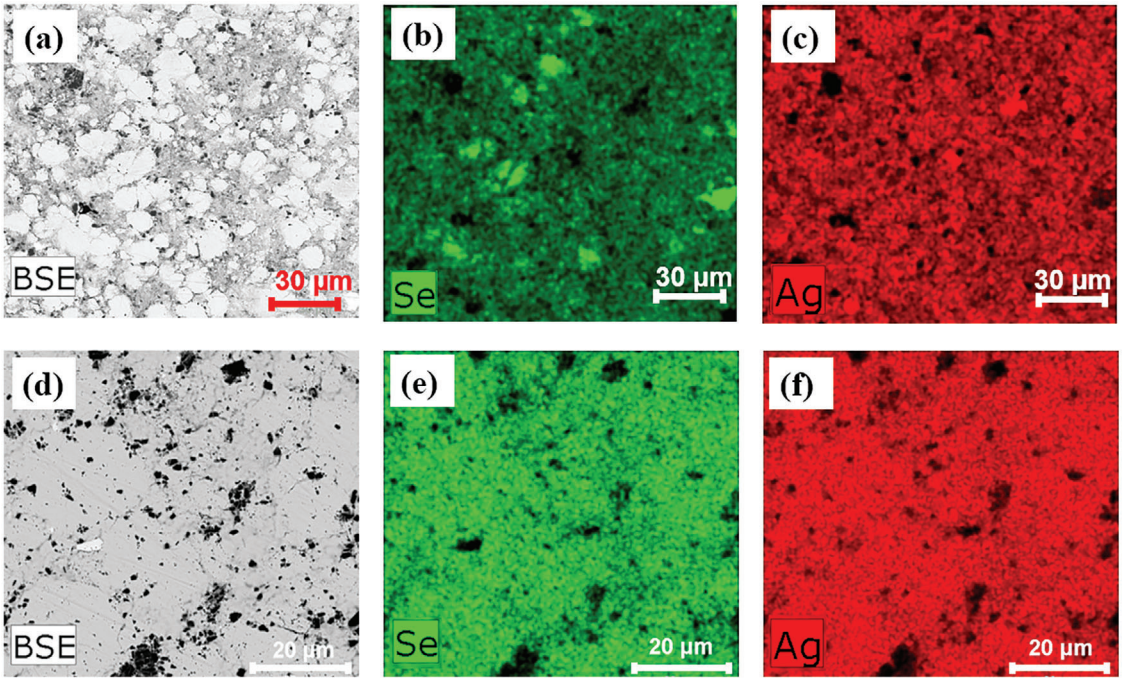


**Figure 3.** Microstructure and chemical distribution of nonsintered and sintered films: BSE images and Ag/Se EDXS maps of the nonsintered sample in (a)–(c) and the sintered film in (d)–(f).


© 2024 The Author(s). Advanced Functional Materials published by Wiley-VCH GmbH

16163028, 0, Downloaded from https://onlinelibrary.wiley.com/doi/10.1002/adfm.202403646 by Karlsruher Institut F., Wiley Online Library on [27/06/2024]. See the Terms and Conditions (https://onlinelibrary.wiley.com/terms-and-conditions) on Wiley Online Library for rules of use; OA articles are governed by the applicable Creative Commons License

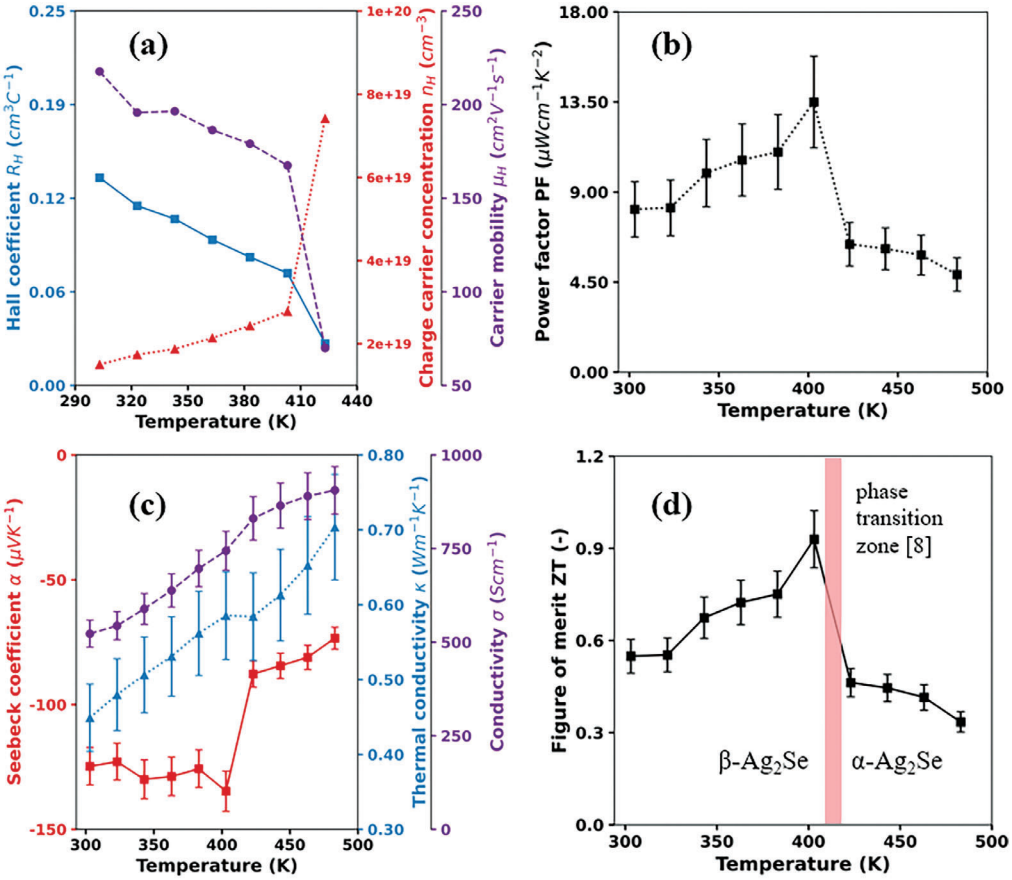


**Figure 4.** Temperature-dependent thermoelectric properties of the printed film after sintering. a) Hall coefficient ($R_H$), Hall carrier concentration ($n_H$), and Hall carrier mobility ($\mu_H$). b) Power factor (PF). c) Electrical conductivity ($\sigma$), Seebeck coefficient ($\alpha$), and thermal conductivity ($\kappa$). d) Figure-of-merit (ZT) of the printed n-type $Ag_2Se$ film.

spin-orbital splitting of d-levels). The binding energy of the Se $3d_{5/2}$ component at 53.4 eV is in good agreement with previously published experiments.[22] The position of the Ag4p peak also corresponds to the $Ag^+$ state. Figure 3 presents both non-sintered and sintered films' microstructural evolution and chemical composition distribution. In the non-sintered film, the backscattered electron (BSE) image of Figure 3a shows distinct material contrasts between the Ag, Se, and $Ag_2Se$ phases. The corresponding elemental maps of Ag and Se in Figure 3b,c exhibit a relatively homogeneous distribution across two phases. However, due to the ball milling process, Ag and Se reacted to form the $Ag_2Se$ phase in some small areas by showing very prominent bright clusters in the elemental maps. Following the sintering process on a hotplate, the thin film undergoes homogenization, transitioning into a nearly single $Ag_2Se$ phase. Consistently, the contrast is reduced, as shown in the BSE image of Figure 3d. Despite some pores and cracks, the EDXS maps of Figure 3e,f reveal a uniform distribution of Ag and Se without any aggregations in the noporous regions. Quantitative analysis of the chemical compositions of the sintered film through EDXS maps (see Figure S1, supporting information,) indicates that Ag constitutes 67.64 at.% (73.98 mass-%), with Se comprising 32.35 at.% (26.01 mass-%), which is in good agreement with the original compositions mixed.

| *Silver/interface material/p-BST* | *Two probe resistivity measurement (Ω), Fluke 289* |
|---|---|
| 1. Silver only | ≈ 8 – 10 Ω |
| 2. $Ag_2Se$ | ≈ 13 Ω |
| 3. Silver/PEDOT nanowires | ≈ 1 Ω |
| 4. Silver/carbon | ≈ 0.4 Ω |
| 5. Silver/graphene | ≈ 0.6 Ω |

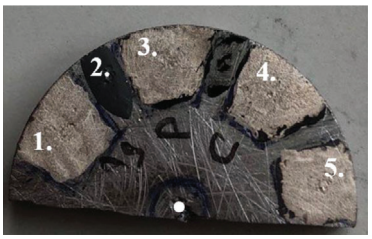


**Figure 5.** Empirical investigation of a suitable printable interface material to lower contact resistances in a printed TEG device. The areas (1,2,3,4,5) of a piece of p-type $Bi_{0.5}Sb_{1.5}Te_3$ ingot were manually painted with silver conductive paste with and without a selection of commercial and self-synthesized interface materials, including $Ag_2Se$, PEDOT nanowires, carbon, and graphene. The two-probe measurement was taken from the center of the conductive silver pads to the center of the ingot, highlighted with a white dot.

### 2.2. Thermoelectric Properties of Printed n-Type Film

The temperature-dependent thermoelectric properties of the printed $Ag_2Se$ film after sintering were studied on a chip (see Figure S2, Supporting Information) using a commercial thin-film analyzer (TFA) setup. **Figure** 4c shows that the


© 2024 The Author(s). Advanced Functional Materials published by Wiley-VCH GmbH

16163028, 0, Downloaded from https://onlinelibrary.wiley.com/doi/10.1002/adfm.202403646 by Karlsruher Institut F., Wiley Online Library on [27/06/2024]. See the Terms and Conditions (https://onlinelibrary.wiley.com/terms-and-conditions) on Wiley Online Library for rules of use; OA articles are governed by the applicable Creative Commons License

electrical conductivity ($\sigma$) increases with increasing temperature, indicating a nondegenerate semiconductor transport behavior. Meanwhile, the absolute value of the Seebeck coefficient ($\alpha$) decreases as temperature rises. To investigate the reason for the change in $\sigma$ and $\alpha$, we also measured the temperature-dependent Hall coefficients ($R_H$). Correspondingly, the variation of Hall carrier concentration ($n_H$) and Hall carrier mobility ($\mu_H$) with temperature were calculated from $R_H$. As shown in Figure 4a, $n_H$ increases with increasing temperature because more electrons contribute to the conductivity at elevated temperatures. In contrast, $\mu_H$ decreases due to stronger scattering of electrons. The drastic change above 400 K is ascribed to the phase transition of $\beta$-$Ag_2Se$ to the $\alpha$-$Ag_2Se$ phase. The power factor was calculated via $\sigma$ and $\alpha$. As shown in Figure 4b, the power factor reaches a maximum value of ≈13 μW $cm^{-1}K^{-2}$ at 400 K. Furthermore, the film exhibits quite low thermal conductivity, where the room temperature thermal conductivity is 0.45 $Wm^{-1}$ $K^{-1}$. This can be attributed to the printed sample's lower mass density than the theoretical density and the reduced heat conduction in the presence of residual organic binders and additives. As a result, the film has a ZT value of 0.52 at room temperature, reaching a peak of 0.92 at 400 K (Figure 4d).

### 2.3. Selection and Investigation of Printable Electrical Interface Materials

Silver is among the most widely used materials in printed electronics today due to its high electrical conductivity at low curing temperatures in an ambient atmosphere. Because of this, in principle, silver qualifies as a good electrode material and is frequently used in printed TEGs. However, many reports show that the contact resistance between printed silver and Bi-Te-based TE legs can be of significant magnitude,[15,16,23] which poses a serious challenge in the field of printed TEG devices. We experienced similar behavior when printing silver or copper directly on $Ag_2Se$ and p-type Sb-Bi-Te films. The exact effects causing these high resistances are difficult to assess. The reasons for this are likely to be the limited contact zones at the interface of the printed films due to high surface roughness and porosity, the inclusion of non-conducting material domains (oxidation layers, polymer binders, and solvent residues), the diffusion of electrode atoms into the TE material domain,[24–26] and chemical or electrochemical reactions that occur during the fabrication or operation of the device. In commercial bulk Bi-TE-based modules a nickel (Ni) layer generally serves as the diffusion barrier. Applying a Ni layer is also a frequently used technique to reduce contact resistances in out-of-plane printed TEG devices.[17,27] In a previous publication, we avoided this issue by contacting the thermoelectric materials directly without using a dedicated electrode material.[13] However, this approach requires compatible thermoelectric materials with sufficient flexibility to maintain the integrity of the TE film when folding in the TE materials domain. To achieve this Rösch et al. printed thin films of PEDOT and $Ti_2S$, each with a thickness of 1.4 μm, and performed folding exclusively in the PEDOT domain. However, for the inorganic devices produced in this study, the significantly higher film thicknesses (13 μm) prevent a sharp bending of the thermoelectric film. For this reason, we tested different printable interface materials regarding compatibility with our manufacturing process and contact resistance. Applying printable carbon, graphene, and self-synthesized PEDOT nanowires as an interface material between the silver paste and a p-type ingot was investigated and compared to a direct contact with silver and $Ag_2Se$ (c.f. **Figure 5**).

A commercial carbon paste (Dycotec DM-CAP-4701S) yielded the lowest contact resistance in this investigation. The synthesis of the PEDOT nanowires follows the route developed by Han and Foulger[28] and the recipe described in the patent by Silas et al.[29] and the graphene ink was prepared according to the procedure of Abdolhosseinzadeh et al.[30] The resistances in Figure 5 were obtained by two probe measurements with a Fluke 289 multimeter.

### 2.4. Fabrication of the Origami TEGs

The fabrication of the printed origami TEGs (**Figure 6e**) follows a four-step screen printing process with intermediate sintering and drying processes followed by an encapsulation and folding process. The device consists of 21 thermocouples with an individual leg size of 8.5 mm × 14.8 mm.

After the preparation of the n- and p-type pastes, the p-BST pattern was printed on 25 μm polyimide (PI) and alternatively on 50 μm polyethylene naphthalate (PEN) foils. The printed pattern was dried for 5 min at 353 K on a hot plate. The dried p-type film was sintered using pulsed photonic curing with a Novacentrix PulseForge 1200. The detailed sintering parameters have been reported previously.[19] After the photonic curing, the complementary Ag—Se-based n-type patterns were printed on the same substrate. The obtained printed film was then sintered in ambient air on a hot plate at 473 K to form the high-performance $Ag_2Se$ n-type phase. A 90-40y/22° SAATILENE Hitex screen with an emulsion over mesh (EOM) of 6–9 μm was used to print both thermoelectric materials. The contacts were realized with a layered structure of carbon and silver to achieve a low-resistant device. First, a commercial carbon paste (Dycotec DM-CAP-4701S) was screen printed to connect the two TE materials, and in a second step, the silver paste was printed with the same layout on top (Figure 6a). The carbon paste thereby ensures a low contact resistance between the silver and the TE legs. For both contacting materials, a SAATILENE Hitex screen with the specifications 125–35y/22° EOM 6–9 μm was used. Origami-inspired folding of the flat printed patterns brings the device from its 2D layout structure to a functional 3D shape for thermal impedance matching.[31] It represents a critical manufacturing step that can significantly impact the power output of the device. The formation of cracks while folding leads to a higher internal device resistance or can even result in a complete breaking of the conductive path. Therefore, the number of folds was minimized to adapt the layout for the Ag-Se and Bi—Sb—Te inorganic films, and only folding between the thermoelectric legs was done (Figure S3, Supporting Information). A laser cutter was used to groove the surface along the folding lines without cutting through the substrate to facilitate the folding further. Before folding, the TE foils were additionally encapsulated (Figure 5c) using a thin, insulating 4 μm black tape that avoided electrical shorting after folding the device. After encapsulating, folding, and compacting the device, we did not experience significant problems with the


© 2024 The Author(s). Advanced Functional Materials published by Wiley-VCH GmbH

16163028, 0, Downloaded from https://onlinelibrary.wiley.com/doi/10.1002/adfm.202403646 by Karlsruher Institut F., Wiley Online Library on [27/06/2024]. See the Terms and Conditions (https://onlinelibrary.wiley.com/terms-and-conditions) on Wiley Online Library for rules of use; OA articles are governed by the applicable Creative Commons License

mechanical stability of the TEG module, when the device was handled with proper care. In Figure S7 (Supporting Information) results of bending tests on the printed film are presented.

### 2.5. Performance of the origami TEGs

Our printing and folding method produced a functional prototype on a 25 µm polyimide and a 50 µm PEN substrate. The p-type Bi-Sb-Te film on the PI substrate could be sintered at higher temperatures due to the higher temperature stability of the PI, resulting in a more performant device. On PI, the device resistance was ≈ 56 Ω, while on PEN, it was ≈ 76 Ω. The device's performance realized on PEN is given in Figure S4 (Supporting Information). The finished devices with 21 thermocouples were characterized using an in-house TEG measurement setup in which the temperature of two copper blocks can be varied between 273 and 363 K. For the measurement, the TEG is clamped between two copper blocks using a guided rail, and heat-conducting paste (FEROTHERM 4) is applied between the copper blocks and the TEG to improve the thermal contact (c.f. **Figure** 7a). The current-voltage characteristic of the TEG is measured with a source measurement unit (Keithley 2601B, SMU) after a stationary temperature difference $\Delta T$ has been established (c.f. Figure 7b).

To make the device performance comparable, the power density was calculated with the cross-section of the device and the TE film, respectively. Therefore, the width of the folded device was measured using a micrometer screw gauge and checked with the results from a white light interferometric (WLI) measurement using a BRUKER Contour GT-K 3D Optical Microscope (see Figure S5, Supporting Information). For the device printed on PI, the total width measured was 0.73 mm, which is in good agreement with the theoretical width of 0.728 mm when the thicknesses of the 14 folded individual layers are summed up with the average thicknesses of the WLI measurement (substrate/25 µm, p-type/13 µm or n-type/13 µm, carbon/5 µm, silver/5 µm, encapsulation/4 µm). The power density calculation uses the measured width (0.73 mm), resulting in a cross-surface area of 34.6 mm$^2$ (0.73 mm × 47.4 mm). The origami TEG has a thermoelectric fill factor of 22.88%, which is the ratio of the TE materials volume compared to the total device volume. The printed origami TEG exhibits a maximum power of 370.88 µW, which relates

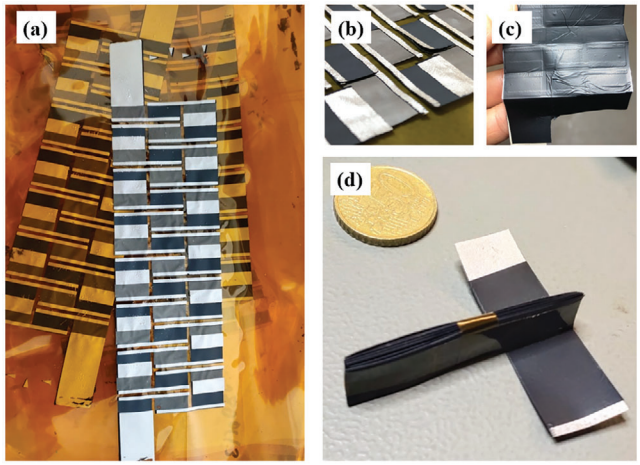


**Figure 6.** a–c) Intermediate manufacturing step of the origami TEG with 21 thermocouples connected in series. d) Functional folded origami TEG with a 50 €$_{ct}$ coin as reference.

to a power density $p_{max}$ of 10.72 Wm$^{-2}$ for a ΔT = 80.7 K (see **Table** 1). This value is among the highest reported power densities for a fully printed TEG that was fabricated in air, omitting compaction processes and sintering steps in a vacuum or inert atmosphere.

## 3. Discussion

### 3.1. The High-Power Output and Scalability of the Printed Origami-TEGs

The successful implementation of printed TEGs for IoT applications depends on many factors, including a high power density $p_{max}$, high power output $P_{MPP}$ and a scalable manufacturing process. While high power densities are achieved for many printed devices, it does not necessarily mean that the device can deliver sufficient power for an IoT application, e.g., when the contact resistances are preventing the printing of a larger number of thermocouples or if the printing thickness is very small. While from an application point of view, the power density

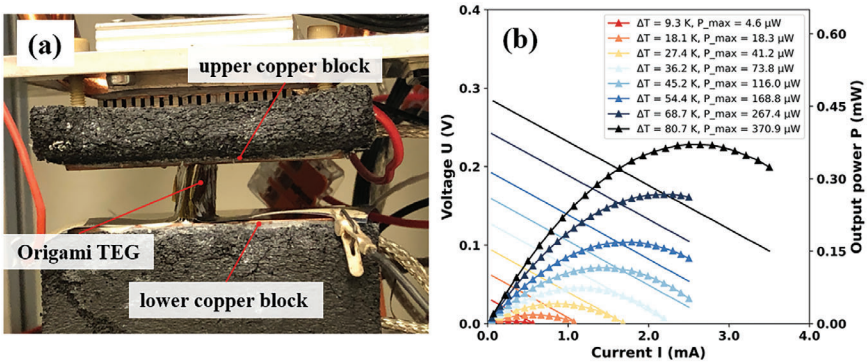


**Figure 7.** a) TEG-Measurement setup for device characterization. A temperature difference can be applied to the device via two copper blocks, each connected to a Peltier module. The resulting *I–V* curve of the TEG can be logged with a source measurement unit (Keithley 2601B SMU). b) Electrical output power and *I–V* curve of the folded origami TEG printed on a PI substrate at different temperature differences. For the measurement, the cold side temperature was fixed at 20 °C.


© 2024 The Author(s). Advanced Functional Materials published by Wiley-VCH GmbH

16163028, 0, Downloaded from https://onlinelibrary.wiley.com/doi/10.1002/adfm.202403646 by Karlsruher Institut F., Wiley Online Library on [27/06/2024]. See the Terms and Conditions (https://onlinelibrary.wiley.com/terms-and-conditions) on Wiley Online Library for rules of use; OA articles are governed by the applicable Creative Commons License

**Table 1.** Comparison of simulated power, power density, and device resistance of a folded TEG on a 25 µm Kapton substrate for different temperature gradients.

| | ΔT | Device resistance | Device power output (MPP) | Power density (device CS) | Power density (TE material CS)* |
|---|---|---|---|---|---|
| | 18.1 K | 56.73 Ω | 18.27 µW | 0.528 $Wm^{-2}$ | 2.3 $Wm^{-2}$ |
| Experimental | 54.4 K | 56.33 Ω | 168.83 µW | 4.88 $Wm^{-2}$ | 21.32 $Wm^{-2}$ |
| | 80.7 K | 55.73 Ω | 370.88 µW | 10.72 $Wm^{-2}$ | 46.84 $Wm^{-2}$ |
| | 18.1 K | 46.68 Ω | 16.9 µW | 0.488 $Wm^{-2}$ | 2.13 $Wm^{-2}$ |
| Simulation | 54.4 K | 46.73 Ω | 168.2 µW | 4.86 $Wm^{-2}$ | 21.24 $Wm^{-2}$ |
| | 80.7 K | 46.62 Ω | 402.8 µW | 11.64 $Wm^{-2}$ | 50.88 $Wm^{-2}$ |

*Note that the final column rates the maximum power point (MPP) for the TE material's cross-sectional (CS) area.

including the substrate is important, **Figure 8a** compares the origami-TEG to other recently reported printed and thin film devices via the normalized power density $\varphi = p_{max}/\Delta T^2$ calculated using the cross-sectional area of the TE material only and the normalized power output. Additionally, $p_{max}$ including the substrate material given in Table 1. For the fabricated device $\varphi$ is found to be relatively constant at 7.04, 7.32, and 7.19 nW $mm^{-2}$ $K^{-2}$ at different ΔT = 18.1, 54.4 and 80.7 K. The maximum value of $\varphi$ for the presented origami-TEG (7.32 nW $mm^{-2}$ $K^{-2}$) is exceptionally high for a fully printed TEG device. To our knowledge, it manifests the highest reported value for a screen-printed device manufactured in the air without an additional cold or hot-pressing step. One important key to this high power density is the application of carbon paste between the silver electrode and the thermoelectric materials as this results in a stable, low ohmic contact resistance in the device. Furthermore, it allows us to adopt a rapid screen-printing method for all active materials in the device and combine it with fast in-air sintering processes (Figure 8c). This results in a significantly shorter overall manufacturing time (Figure 8b), allowing a fast and scalable production of the origami TEG.

### 3.2. Comparison of Experimental and Simulated Results

To determine the potential power output under thermally impedance-matched conditions, a simulation model was built using COMSOL Multiphysics 6.2.

Therefore, a representative part of the 3D model consisting of three thermoelectric couples (two folded strips) was modeled considering the device symmetry and repetition (**Figure 9a**). For each relevant component (substrate, p- and n-type material, carbon interface, conducting silver, encapsulation foil, heat source, and heat sink), the experimentally determined material properties were used as input parameters for the simulation. Subsequently, as heat transfer boundary conditions, three distinct hot side temperatures $T_h$ = 311.1, 347.4, 373.7 K with a constant $T_c$ = 293 K cold side temperature were applied at the respective copper block source and sink. A thermal insulance of $R_{th}$ = 0.002 $m^2$ $KW^{-1}$ was additionally applied at the two interfaces between the copper blocks and the device surfaces. Following the thermal boundary conditions, the electric boundary conditions were applied to the conductor's terminals, one being ground and the other as an active terminal. While for the

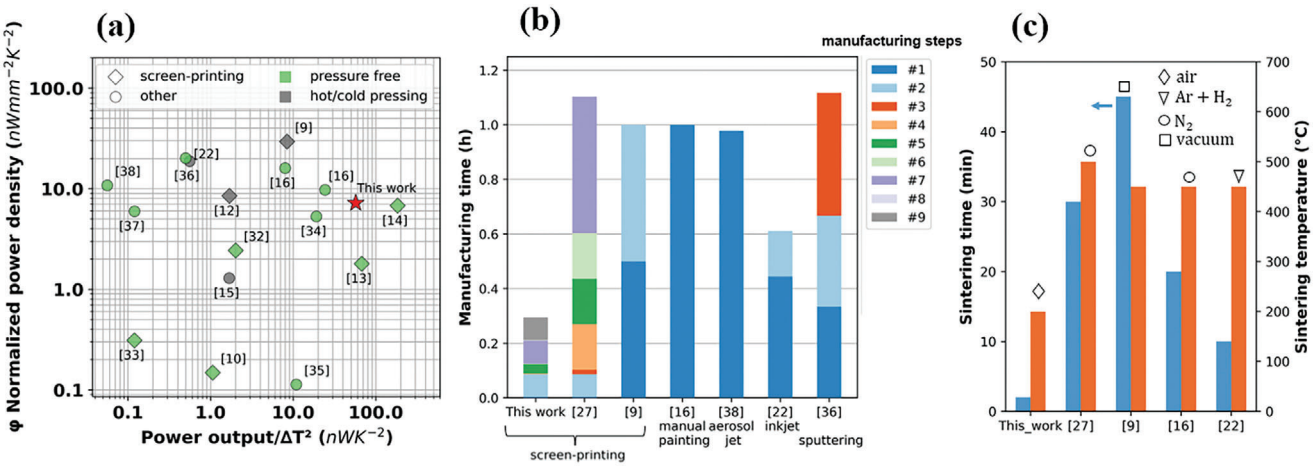


**Figure 8.** a) Comparison of the normalized power density for different thin/thick film in-plane printed devices based on BiTe and $Ag_2Se$ manufactured via screen-printing,[9,10,12–14,32,33] manual painting,[16] dispenser printing,[34] drop casting,[35] blade-coating,[15] sputtering,[36] inkjet printing,[22,37] and aerosol jet printing[38] with and without a hot/cold pressing manufacturing step. b) Comparison of the manufacturing time of several high power density devices produced with different printing techniques,[9,16,22,27,36,38] c) Sintering time, temperature, and atmosphere for different printed TE films. *Note (b) only includes the manufacturing steps, for which time information is provided in the publication.

 © 2024 The Author(s). Advanced Functional Materials published by Wiley-VCH GmbH

16163028, 0, Downloaded from https://onlinelibrary.wiley.com/doi/10.1002/adfm.202403646 by Karlsruher Institut F., Wiley Online Library on [27/06/2024]. See the Terms and Conditions (https://onlinelibrary.wiley.com/terms-and-conditions) on Wiley Online Library for rules of use; OA articles are governed by the applicable Creative Commons License

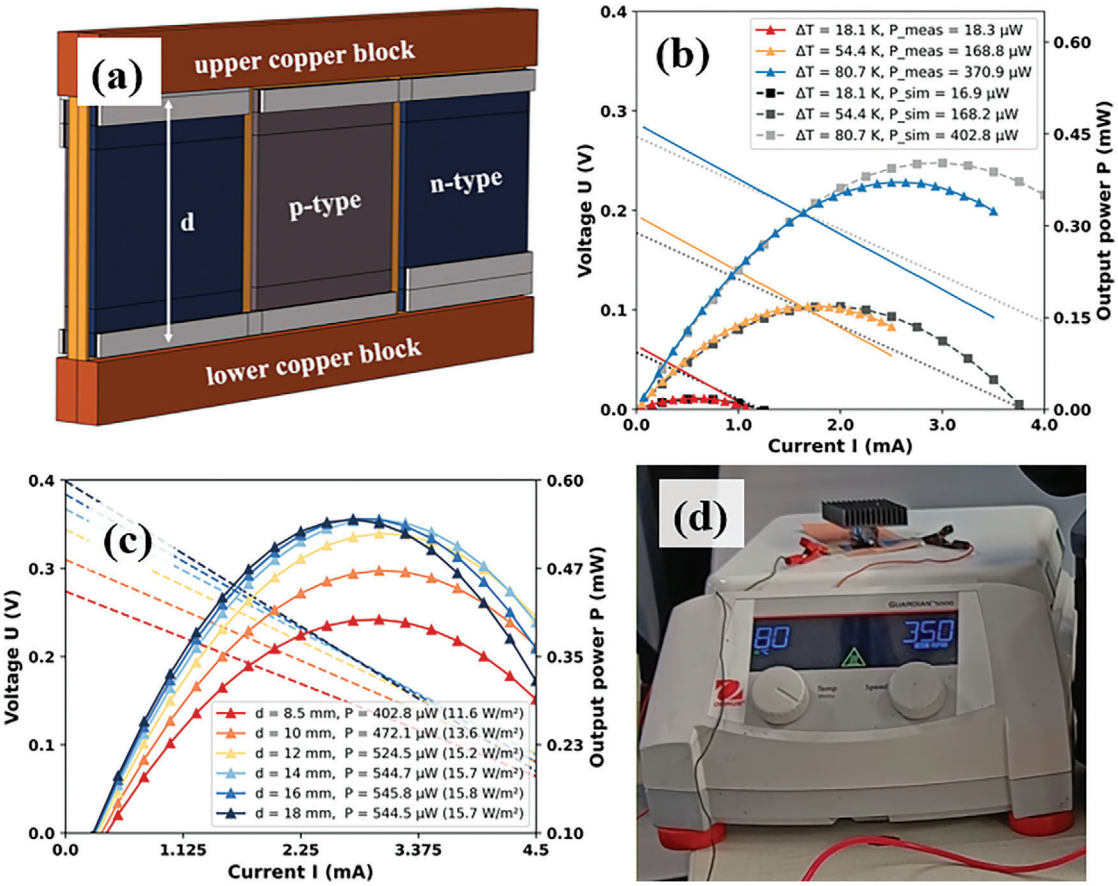


**Figure 9.** a) COMSOL model of a representative section of the printed origami TEG in the measurement setup. b) Comparison of the measured and simulated values. c) The COMSOL simulation shows the optimum leg length and device height under thermally impedance-matched conditions. The resulting *I–V* curves indicate that the device power is increasing until a leg length between 16 and 18 mm with a maximum of 545.8 μW (ΔT = 80.7 K). For longer legs, the device power decreases. d) One origami TEG module positioned on a hot plate delivers power for IoT power management.

electric domains in the model (p- and n-type legs, interface material, and conductor material), Joule heating is applied to all domains; the thermoelectric effect is only considered for the p- and n-type legs. To determine the maximum power point (MPP), the current was varied from 0 to 5 mA in steps of 0.1 mA. Figure 8c compares the simulated and measured data. At low electrical currents, the measured power exceeds the simulated one due to the higher output voltage of the measured device; at high ΔT, the simulated power is larger due to the underestimated device resistance. However, in the relevant regions around the MPP, the error between simulation and measured data is below 10%, which shows a good agreement between the simulation model and real device performance (Figure 9b). This simulation model was then used to determine the optimum leg length (*d*) at which the output power is maximized. Our simulation in Figure 9c indicates that the leg length can be increased up to 18 mm, indicating further optimization potential of our TEG. Furthermore, to evaluate the optimization potential of the interface layer, we replaced the carbon interface with silver in the simulation model, which resulted in a reduced device resistance of 37.3 Ω.

### 3.3. Supplying a Power Electronic with the Origami TEG

To effectively power IoT devices, the TEG's voltage must be amplified to a level compatible with the requirements of conventional electronics. Therefore, one origami TEG module printed on PEN was positioned above a hot plate with a passive heatsink on top (Figure 9d) and connected to a power management comprising a two-stage amplification chain (see Figure S6b-a, Supporting Information). The 1st stage contains a DC–DC resonant converter, a modification of an Armstrong oscillator adapted from Adami et al.,[28] and acts as a startup stage for the LTC3108[39] boost converter. For the 2nd stage, a MAX17220 boost converter is employed to further amplify the output voltage from the initial stage to the desired level. With this configuration, the whole circuit generated a regulated output of 2 V when the hotplate was at 80 °C (ΔT = 56 K) (see Figure S6b-b, Supporting Information). Despite a mismatch in the resistances of the boost converter and the origami TEG, which did not allow for maximum power transfer, the experiment demonstrated that the origami TEG could be used to power a low-power application, like an atmospheric sensor along with a low-power microcontroller,


© 2024 The Author(s). Advanced Functional Materials published by Wiley-VCH GmbH

16163028, 0, Downloaded from https://onlinelibrary.wiley.com/doi/10.1002/adfm.202403646 by Karlsruher Institut F., Wiley Online Library on [27/06/2024]. See the Terms and Conditions (https://onlinelibrary.wiley.com/terms-and-conditions) on Wiley Online Library for rules of use; OA articles are governed by the applicable Creative Commons License

with BLE or NFC capabilities. The Figure S6 (Supporting Information) provides a more detailed description of the power management architecture and the experiment with the origami TEG.

## 4. Conclusion

In conclusion, our study presents a novel, fully printed origami TEG module that shows significant advancements in power output, power density, and manufacturing of printed TEGs. A key focus of this work has been on scalable manufacturing using screen printing for the thermoelectric and the contact materials. For this, we synthesized a pair of high-performance printable TE materials (n-type $Ag_2Se$ and p-type Bi-Sb-Te) and fabricated a rectangular cuboid TEG module with the dimensions 0.73 mm × 47.7 mm × 8.5 mm (width × length × height) comprising of 21 thermocouples with a thermoelectric fill factor of 22.88%. For the means of thermal impedance matching, the manufacturing included an origami folding process, resulting in the heat flowing in-plane along the height (8.5 mm) of the device. Using a simulation model, we demonstrated that the device performance can be further improved by increasing the device's height. Furthermore, we employed a carbon-based printed diffusion barrier between the TE materials and the printed silver contacts to minimize contact resistances. As a result, the printed TEG module exhibits a particularly low resistance of 56 Ω and can deliver 370.88 µW at a ΔT of 80.7 K and 73.8 µW at a more moderate ΔT of 36.2 K. Furthermore, we used an origami TEG to supply power for a dedicated power management for an IoT sensor. These results demonstrate the potential of printed TEGs as an effective alternative for powering the Internet of Things.

## 5. Experimental Section

*Materials*: Ag powder (2-3.5 µm, Sigma Aldrich), Se powder (100 mesh, ≥99.5% trace metals basis, Sigma Aldrich), Ingot of p-type $Bi_{0.5}Sb_{1.5}Te_3$ (EVERREDtronics), Copper powder (spheroidal, 10–25 µm, 98%, Sigma-Aldrich), Polyvinylpyrrolidone (PVP) (average Mw ≈40 000, Sigma Aldrich), N-methyl-2-pyrrolidone (NMP) (anhydrous, 99.5%, Sigma-Aldrich), Polyethylenenaphtalate (PEN, 50 µm), Kapton polyimide (DuPont), Silver ink (LOCTITE ECI 1010 E&C), Carbon paste (Dycotec DM-CAP-4701S), Heat conductive paste (IBF-FEROTHERM 4).

*Preparation, Printing, and Sintering of TE Films*: Preparing the printable n-type Ag-Se and the p-type Bi-Sb-Te pastes follows an in-house developed one-pot synthesis. Two cups of a planetary ball mill (Fritsch Pulverisette 5 Premium Line) were filled with thermoelectric powders, binders, and solvents. For the n-type paste, the stoichiometric ratio of 2:1 ($Ag_2Se$) of elemental Ag powder and Se powder was filled in a ball mill cup, and for the p-type ground $Bi_{0.5}Sb_{1.5}Te_3$ (p-BST) powder was mixed with 5 wt% of inorganic binder (IB) containing elemental Cu and Se powders as described in the previous report.[13] The two powders were mixed with a solvent-binder solution of PVP dissolved in NMP. After purging the cups with nitrogen, the mixture underwent ball milling for 45 min at 200 rpm. Next, the printed n-type film was prepared to study its thermoelectric properties. The printed n-type film was dried at 373 K for 5 min), and sintered on a hotplate in an ambient atmosphere at 473 K for 5 min. A fully printed Origami-TEG was fabricated using the printed $Ag_2Se$-based TE material for n-type legs and previously reported Bi-Sb-Te-based printed TE material for p-type legs. A screen (90–40y/22° SAATILENE Hitex, EOM 6–9 µm) was used to print both thermoelectric materials to achieve a thick film. The printing was conducted on a semi-automatic flatbed screen-printing machine (ROKUPRINT SD 05) using screens with a dimension of 600 × 300 mm.

*Characterization for the Printed Materials and the Origami TEG*: Crystallographic structures and phases of the printed n-type films were determined by the X-ray diffraction (XRD) technique in Bragg–Brentano geometry using Ni-filtered Cu-K$\alpha$1,2 lines on a Bruker D8 diffractometer with a Lynxeye XE detector and an Anton Paar HTK1200 heating chamber. The XPS measurements were carried out under an ultra-high vacuum with a base pressure of $1 \times 10^{-9}$ mbar. Core-level spectra were recorded under normal emission using Al-K$\alpha$ radiation (1486.6 eV) with a Scienta R4000 hemispherical electron analyzer (the instrumental resolution is ≈1.3 eV). First, the survey XP spectrum was measured and in addition to expected Ag/Se peaks, only weak C1s and O1s peaks were observed, resulting from carbon/oxygen surface contamination. Then, the detailed Ag3d and combined Se3d+Ag4p XP spectra were recorded. For a precise determination of the Ag3d and Se3d/Ag4p-lines position and necessary correction, the CasaXPS software was used. The line correction was adjusted to the O1s peak at 532 eV. All spectra were fitted with Voigt profile (10% of Lorentz contribution) using Shirley background for the Ag3d and Se3d peaks and linear background for the Ag4p peak. The microstructure and composition distribution of both nonsintered and sintered n-type printed films were investigated using the FEI Quanta 650 environmental scanning electron microscope (SEM), which was equipped with a Schottky field emitter and a backscattered electron (BSE) detector. Additionally, Energy Dispersive X-ray Spectroscopy (EDXS) measurement was employed with a Bruker EDXS Quantax 400 and a solid-state detector, operating at a voltage of 15 keV. The temperature-dependent electrical conductivity ($\sigma$), Seebeck coefficient ($\alpha$), and thermal conductivity ($\kappa$) of the printed n-type $Ag_2Se$ film were determined using a Linseis thin film analyzer (TFA) system. The associated relative errors for $\alpha$, $\sigma$, and $\kappa$ measurements were 7%, 6%, and 10% respectively.

The Hall coefficients (RH), Hall carrier concentration (nH), and Hall carrier mobility (µH) of the film with temperature were studied using a Linseis HCS 10 instrument.

The performance of the printed Origami TEG was analyzed using maximum power point (MPP) tracking with a KEITHLEY Source Measuring Unit 2601. The details of the device characterization setup are described in the supplementary information of a previous publication by Rösch et al.[13]

Thickness measurements on the printed films and device were done with a micrometer screw gauge and a white light interferometric (WLI) measurement was done using a BRUKER Contour GT-K 3D Optical Microscope.

## Supporting Information

Supporting Information is available from the Wiley Online Library or from the author.

## Acknowledgements

This project is funded by the Federal Ministry of Education and Research (BMBF) and the Baden-Württemberg Ministry of Science as part of the Excellence Strategy of the German Federal and State Governments. The authors wish to acknowledge the Deutsche Forschungsgemeinschaft (DFG, German Research Foundation) under Germany's Excellence Strategy via the Excellence Cluster 3D Matter Made to Order (EXC-2082/1 – 390761711), the BMBF through project 03INT606AG and the BMWi through WIPANO project 03THWBW004 for financial support. The authors wish to acknowledge funding by the Ministry of Science, Research, and Arts of the Federal State of Baden Württemberg through the MERAGEM graduate school. The German Federal Environmental Foundation (Deutsche Bundesstiftung Umwelt – DBU), through the DBU Ph.D. scholarship program, also supported this work. This project has received funding from the European Union's Horizon 2020 research and innovation program under grant agreement no. 814945—SolBio-Rev, under the Marie Skłodowska-Curie grant agreement No. 955837 – HORATES, and the authors acknowledge funding by the European Research Council, grant 101097876 – ORTHOGONAL.

Open access funding enabled and organized by Projekt DEAL.


© 2024 The Author(s). Advanced Functional Materials published by Wiley-VCH GmbH

16163028, 0, Downloaded from https://onlinelibrary.wiley.com/doi/10.1002/adfm.202403646 by Karlsruher Institut F., Wiley Online Library on [27/06/2024]. See the Terms and Conditions (https://onlinelibrary.wiley.com/terms-and-conditions) on Wiley Online Library for rules of use; OA articles are governed by the applicable Creative Commons License

## Conflict of Interest

The authors declare no conflict of interest.

## Data Availability Statement

The data that support the findings of this study are available from the corresponding author upon reasonable request.

## Keywords

$Ag_2Se$, $Bi_{0.5}Sb_{1.5}Te_3$, folded electronics, interface engineering, IoT, origami thermoelectric generator, printed electronics, TEG

Received: February 29, 2024
Revised: May 24, 2024
Published online:

[1] C. Forman, I. K. Muritala, R. Pardemann, B. Meyer, *Renew. Sustain. Energy Rev.* **2016**, *57*, 1568.
[2] M. Graef, in *2021 IEEE International Roadmap for Devices and Systems Outbriefs*, IEEE, Santa Clara, CA **2021**, pp. 1–47.
[3] V. Leonov, T. Torfs, P. Fiorini, C. Van Hoof, *IEEE Sens. J.* **2007**, *7*, 650.
[4] M. Burton, G. Howells, J. Atoyo, M. Carnie, *Adv. Mater.* **2022**, *34*, 2108183.
[5] M. Zeng, D. Zavanelli, J. Chen, M. Saeidi-Javash, Y. Du, S. LeBlanc, G. J. Snyder, Y. Zhang, *Chem. Soc. Rev.* **2022**, *51*, 485.
[6] A. Sarbajna, A. G. Rösch, L. Franke, U. Lemmer, M. M. Mallick, *Adv. Eng. Mater.* **2023**, *25*, 2200980.
[7] S. Shin, R. Kumar, J. W. Roh, D.-S. Ko, H.-S. Kim, S. I. Kim, L. Yin, S. M. Schlossberg, S. Cui, J.-M. You, S. Kwon, J. Zheng, J. Wang, R. Chen, *Sci. Rep.* **2017**, *7*, 7317.
[8] M. M. Mallick, A. G. Rösch, L. Franke, S. Ahmed, A. Gall, H. Geßwein, J. Aghassi, U. Lemmer, *ACS Appl. Mater. Interfaces* **2020**, *12*, 19655.
[9] T. Varghese, C. Dun, N. Kempf, M. Saeidi-Javash, C. Karthik, J. Richardson, C. Hollar, D. Estrada, Y. Zhang, *Adv. Funct. Mater.* **2020**, *30*, 1905796.
[10] M. M. Mallick, L. Franke, A. G. Rösch, S. Ahmad, H. Geßwein, Y. M. Eggeler, M. Rohde, U. Lemmer, *ACS Appl. Mater. Interfaces* **2021**, *13*, 61386.
[11] M. M. Mallick, A. Sarbajna, A. G. Rösch, L. Franke, H. Geßwein, Y. M. Eggeler, U. Lemmer, *Appl. Mater. Today* **2022**, *26*, 101269.
[12] T. Varghese, C. Hollar, J. Richardson, N. Kempf, C. Han, P. Gamarachchi, D. Estrada, R. J. Mehta, Y. Zhang, *Sci. Rep.* **2016**, *6*, 33135.
[13] A. G. Rösch, A. Gall, S. Aslan, M. Hecht, L. Franke, M. M. Mallick, L. Penth, D. Bahro, D. Friderich, U. Lemmer, *npj Flex. Electron.* **2021**, *5*, 1.
[14] C. Zeng, K. Chen, C. Koz, E.-C. Stefanaki, E. S. S. Galindez, H. Zhang, O. Fenwick, R. Tuley, E. Bilotti, *Nano Energy* **2023**, *121*, 109213.
[15] Y. Tian, I. Florenciano, H. Xia, Q. Li, H. E. Baysal, D. Zhu, E. Ramunni, S. Meyers, T.-Y. Yu, K. Baert, T. Hauffman, S. Nider, B. Göksel, F. Molina-Lopez, *Adv. Mater.* **2023**, *36*, 2307945.
[16] S. H. Park, S. Jo, B. Kwon, F. Kim, H. W. Ban, J. E. Lee, D. H. Gu, S. H. Lee, Y. Hwang, J.-S. Kim, D.-B. Hyun, S. Lee, K. J. Choi, W. Jo, J. S. Son, *Nat. Commun.* **2016**, *7*, 13403.
[17] S. J. Kim, H. E. Lee, H. Choi, Y. Kim, J. H. We, J. S. Shin, K. J. Lee, B. J. Cho, *ACS Nano* **2016**, *10*, 10851.
[18] M. M. Mallick, A. G. Rösch, L. Franke, A. Gall, S. Ahmad, H. Geßwein, A. Mazilkin, C. Kübel, U. Lemmer, *J. Mater. Chem. A* **2020**, *8*, 16366.
[19] M. M. Mallick, L. Franke, A. G. Rösch, H. Geßwein, Z. Long, Y. M. Eggeler, U. Lemmer, *Adv. Sci.* **2022**, *9*, 2202411.
[20] D. Yang, X. Su, F. Meng, S. Wang, Y. Yan, J. Yang, J. He, Q. Zhang, C. Uher, M. G. Kanatzidis, X. Tang, *J. Mater. Chem. A* **2017**, *5*, 23243.
[21] W. Wang, Y. Geng, Y. Qian, M. Ji, Y. Xie, *Mater. Res. Bull.* **1999**, *34*, 877.
[22] Y. Liu, Q. Zhang, A. Huang, K. Zhang, S. Wan, H. Chen, Y. Fu, W. Zuo, Y. Wang, X. Cao, L. Wang, U. Lemmer, W. Jiang, *Nat. Commun.* **2024**, *15*, 2141.
[23] F. Kim, B. Kwon, Y. Eom, J. E. Lee, S. Park, S. Jo, S. H. Park, B.-S. Kim, H. J. Im, M. H. Lee, T. S. Min, K. T. Kim, H. G. Chae, W. P. King, J. S. Son, *Nat. Energy* **2018**, *3*, 301.
[24] R. O. Carlson, *J. Phys. Chem. Solids* **1960**, *13*, 65.
[25] H. P. Dibbs, J. R. Tremblay, *J. Appl. Phys.* **1968**, *39*, 2976.
[26] J. D. Keys, H. M. Duttont, *J. Phys. Chem. Solids* **1963**, *24*, 563.
[27] S. J. Kim, J. H. We, B. J. Cho, *Energy Environ. Sci.* **2014**, *7*, 1959.
[28] M. G. Han, S. H. Foulger, *Small* **2006**, *2*, 1164.
[29] S. M. Aslan, A. Gall, P. Lieber, U. Lemmer, S. Bräse, EP3587521A1, **2018**.
[30] S. Abdolhosseinzadeh, C. (John) Zhang, R. Schneider, M. Shakoorioskooie, F. Nüesch, J. Heier, *Adv. Mater.* **2022**, *34*, 2103660.
[31] A. G. Rösch, L. Franke, M. M. Mallick, U. Lemmer, *Energy Convers. Manag.* **2023**, *279*, 116776.
[32] J. Feng, W. Zhu, Z. Zhang, L. Cao, Y. Yu, Y. Deng, *ACS Appl. Mater. Interfaces* **2020**, *12*, 16630.
[33] Z. Cao, E. Koukharenko, M. J. Tudor, R. N. Torah, S. P. Beeby, *J. Phys. Conf. Ser.* **2013**, *476*, 012031.
[34] D. Madan, Z. Wang, A. Chen, R. Winslow, P. K. Wright, J. W. Evans, *Appl. Phys. Lett.* **2014**, *104*, 013902.
[35] H. Fang, B. C. Popere, E. M. Thomas, C.-K. Mai, W. B. Chang, G. C. Bazan, M. L. Chabinyc, R. A. Segalman, *J. Appl. Polym. Sci.* **2017**, *134*, app44208.
[36] D.-W. Ao, W.-D. Liu, Z.-H. Zheng, X.-L. Shi, M. Wei, Y.-M. Zhong, M. Li, G.-X. Liang, P. Fan, Z.-G. Chen, *Adv. Energy Mater.* **2022**, *12*, 2202731.
[37] B. Chen, M. Kruse, B. Xu, R. Tutika, W. Zheng, M. D. Bartlett, Y. Wu, J. C. Claussen, *Nanoscale* **2019**, *11*, 5222.
[38] M. Saeidi-Javash, W. Kuang, C. Dun, Y. Zhang, *Adv. Funct. Mater.* **2019**, *29*, 1901930.
[39] Ultralow Voltage Step-Up Converter and Power Manager, LTC3108, Rev. D, Analog Devices, 03/2019. Available: https://www.analog.com/media/en/technical-documentation/data-sheets/LTC3108.pdf.


© 2024 The Author(s). Advanced Functional Materials published by Wiley-VCH GmbH

16163028, 0, Downloaded from https://onlinelibrary.wiley.com/doi/10.1002/adfm.202403646 by Karlsruher Institut F., Wiley Online Library on [27/06/2024]. See the Terms and Conditions (https://onlinelibrary.wiley.com/terms-and-conditions) on Wiley Online Library for rules of use; OA articles are governed by the applicable Creative Commons License